International Journal of Minerals, Metallurgy and Materials
Volume 30, Number 8, August 2023, Page 1502
https://doi.org/10.1007/s12613-023-2617-6

Experiment on acoustic emission response and damage evolution characteristics of polymer-modified cemented paste backfill under uniaxial compression

Shenyang Ouyang[1)], *Yanli Huang*[1,2),✉], *Nan Zhou*[1)], *Ming Li*[1,3)], *Xiaotong Li*[1)], *Junmeng Li*[1)], *Fei Ke*[1)], *and Yahui Liu*[1)]

1) State Key Laboratory of Coal Resources and Safe Mining, School of Mines, China University of Mining and Technology, Xuzhou 221116, China
2) Xinjiang Institute of Engineering, Urumqi 830000, China
3) Henan Energy Chemical Group Co., Ltd., Zhengzhou 450000, China
(Received: 13 September 2022; revised: 20 February 2023; accepted: 21 February 2023)

Abstract: The mechanical properties of cemented paste backfill (CPB) determine its control effect on the goaf roof. In this study, the mechanical strength of polymer-modified cemented paste backfill (PCPB) samples was tested by uniaxial compression tests, and the failure characteristics of PCPB under the compression were analyzed. Besides, acoustic emission (AE) technology was used to monitor and record the cracking process of the PCPB sample with a curing age of 28 d, and two AE indexes (rise angle and average frequency) were used to classify the failure modes of samples under different loading processes. The results show that waterborne epoxy resin can significantly enhance the mechanical strength of PCPB samples (when the mass ratio of polymer to powder material is 0.30, the strength of PCPB samples with a curing age of 28 d is increased by 102.6%); with the increase of polymer content, the mechanical strength of PCPB samples is improved significantly in the early and middle period of curing. Under uniaxial load, the macro cracks of PCPB samples are mostly generated along the axial direction, the main crack runs through the sample, and a large number of small cracks are distributed around the main crack. The AE response of PCPB samples during the whole loading process can be divided into four periods: quiet period, slow growth period, rapid growth period, and remission period, corresponding to the micro-pore compaction stage, elastic deformation stage, plastic deformation stage, and failure instability stage of the stress–strain curve. The AE events are mainly concentrated in the plastic deformation stage; both shear failure and tensile failure occur in the above four stages, while tensile failure is dominant for PCPB samples. This study provides a reference for the safety of coal pillar recovery in pillar goaf.

Keywords: polymer; cemented paste backfill; mechanical strength; acoustic emission

1. Introduction

The goaf with coal pillars is common in the mining area of Western China [1]. After long-term creep, weathering, and other weakening effects, the instability of the coal pillar in the goaf occurs, which can cause large-area roof falling, mine earthquakes, and mine disasters [2–3]. In this case, the safety of the mining area is threatened, and the coordinated development of the mining industry and ecological environment is restricted. Cemented backfill mining technology is the most effective method to control the roof in the goaf. It not only improves the stability of the goaf, but also recovers the remaining coal pillar resources (Fig. 1) [4–6]. However, the strength of conventional cemented backfilling materials is relatively low, which cannot meet the strength requirements of coal pillar extraction in cemented backfill mining [7–11].

In recent years, researchers have systematically studied the mechanical strength and damage characteristics of cemented paste backfill (CPB) [12–15]. Research on the effects of slurry concentration, cement content and type, fly ash content, gangue particle size, and curing age on the mechanical strength of CPB has been widely investigated [16–19]. The previous study has reported that increasing the cement content is the most effective way to improve CPB strength, while this method will greatly increase the mining cost [20–21]. In addition, CPB has a low tensile property and is prone to cracking under high stress, thus weakening the bearing capacity [22]. Fly ash is the waste produced by coal-fired power plants and is mainly composed of alumina and silica. It is a potentially active pozzolanic material. Activator or pretreatment can be used to improve the activity of fly ash and hydration production, then a small amount of C–S–H, C–A–C–H, and other hydration products can be generated; as a result, the uniaxial compressive strength (UCS) of CPB is improved and the amount of cement can be reduced [23–24]. Although this method can meet the strength requirements of large-scale backfilling mining in underground goaf within a certain range, the common cement-based composite material

✉ Corresponding author: Yanli Huang E-mail: 5306@cumt.edu.cn

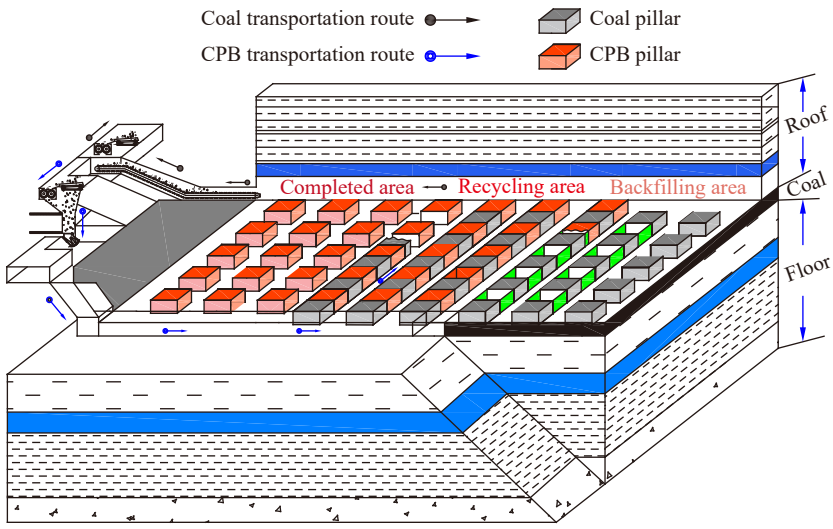

Fig. 1. Schematic diagram of coal pillar recovered by cemented paste backfill in pillar goaf.

has significant shrinkage and brittleness. These features can induce safety risks and threaten the coal pillar recovery of pillar-cemented backfilling mining. In other words, the strength requirements of the common cement-based composite cannot satisfy the coal pillar recovery from the pillar goaf [25–26].

The use of additives is an effective method to improve the properties of ordinary cement-based materials. As a high-efficiency binder with both environmental protection and economic benefits, polymers are widely used as modifiers of cement-based materials. The existing research has shown that polymer-modified cement mortar can enhance the strength and bonding performance of cement-based materials, and polymer can also effectively improve the durability of cement-based materials [27–28]. Moreover, research on the modification mechanism, microstructure, mechanical strength, and application scenarios of polymer-modified mortar has been widely conducted [29–30]. The polymer can fill its internal pores and form a dense structure in the mortar, which ensures the polymer-modified cement-based materials have outstanding waterproof performance, impermeability, water retention, high flexibility, and acid corrosion resistance [31–32]. Zhang *et al.* (2021) [33] illustrated the applications and prospects of polymer-modified cement mortars. Naseem *et al.* (2022) [34] studied the microstructure and mechanical performance of polymer-modified cement composites. Liu *et al.* (2022) [35] modified the aggregate–cement slurry interface with polymers to enhance the mechanical properties of concrete. Liu *et al.* (2021) [36] developed a mechanical strong polymer–cement composite fabricated by *in situ* polymerization within the cement matrix. As one of the most widely used polymers, waterborne epoxy resin emulsion has a wide application range, simple operation, and excellent bonding properties [37–38]. After being dissolved in water, the polymerization reaction can occur and cure at room temperature and high alkaline environment. After curing, a more stable three-dimensional network structure can be formed and interspersed in the cement matrix, greatly improving the performance of the composite material [39]. Xu *et al.* (2022) [40] evaluated the performance of waterborne epoxy resin-modified emulsified asphalt mixtures for asphalt pavement pothole repair. Li *et al.* (2022) [41] studied the effect of waterborne epoxy resins on the hydration kinetics and performance of cement blends. Abdukadir *et al.* (2022) [42] tested the performance of waterborne epoxy resin-based modified liquid asphalt mixtures. Wang *et al.* (2022) [43] studied the effects of polyaniline/lignin composites on the performance of waterborne polyurethane coating for protecting cement-based materials. To sum up, the improvement effect and modification mechanism of water-based epoxy resins on cement-based composites have been deeply understood. However, research on the application of polymers in the backfill materials of the goaf in a coal mine has been rarely reported. In particular, the mechanical strength of polymer-modified cement-based materials and the damage characteristics during load-bearing compression have not been studied.

In this study, the UCS and acoustic emission (AE) tests were carried out on PCPB samples, the influence law of mechanical strength of PCPB was studied, and the macro crack development law of PCPB samples was analyzed. With the aid of the AE monitoring system, the damage characteristics of the meso-structure in the PCPB samples were determined, and the two AE indexes method was used to clarify the failure modes of PCPB samples at different loading stages. The research results provide a scientific and powerful theoretical basis for the development of backfill mining technology and the safe recovery of coal pillars in pillar goaf.

2. Materials and methods

2.1. Raw materials

2.1.1. Gangue

In this test, the waste coal gangue taken from a coal mine was used as the filling aggregate. In order to meet the transportation requirements of the filling slurry, a crusher was used to crush coal gangue with a particle size of 0–10 mm. The X-ray fluorescence (XRF) results show that the main

components of the gangue are SiO_2 (65.23wt%), Al_2O_3 (16.48wt%), Fe_2O_3 (7.14wt%), CaO (2.06wt%), and K_2O (1.68wt%).

2.1.2. Fly ash

The fly ash was obtained from the screened tertiary fly ash of a coal-fired power plant. The XRF results show that the main components of the fly ash are SiO_2 (47.36wt%), Al_2O_3 (25.40wt%), Fe_2O_3 (5.62wt%), CaO (15.05wt%), and MgO (1.92wt%).

2.1.3. Cement

According to the Chinese national standard GB175-2007, the No. 42.5 ordinary portland cement produced by Xuzhou Zhonglian Cement Co., Ltd was used as the cementitious material. The XRF results show that the main components of fly ash are SiO_2 (15.16wt%), Al_2O_3 (17.35wt%), Fe_2O_3 (12.50wt%), CaO (43.50wt%), and MgO (2.35wt%).

2.1.4. Water

The deionized pure water produced by Kunshan Anote Water Treatment Equipment Co., Ltd. was used as the mixed water in the test.

2.1.5. Polymer

The DY-128-50 waterborne epoxy resin lotion and DY-175 waterborne epoxy curing agent, which were produced by Shenyang Dongyan Coating Decoration Co., Ltd., were prepared as the polymer at the dosage ratio of 1:0.8. The water was used as diluent for the polymer. The appearance of waterborne epoxy resin lotion was milky white, and the waterborne epoxy curing agent was a white transparent liquid. Table 1 shows the effective components and characteristics of the polymer.

Table 1. Related parameters of polymer

Name	Type	pH	Density / ($t \cdot m^{-3}$)	Content / wt%
Waterborne epoxy lotion	DY-128-50	6–8	1.05	46.9
Waterborne epoxy curing agent	DY-175	9.5–10.5	1.05	50

2.2. Sample preparation

In the sample preparation, the W-C ratio refers to the mass ratio of water to powder material, the C-G ratio refers to the mass ratio of powder material to gangue, the FA-B ratio refers to the mass ratio of fly ash to binder (cement), and the P-C ratio refers to the mass ratio of polymer to powder material. To study the influence of polymer on the mechanical strength and damage characteristics of CPB, the influence of the P-C ratio on the properties of CPB samples based on the well-applied ratio of backfilling materials (the W-C ratio is 0.5, C-G ratio is 0.4, and FA-B ratio is 0.6) was discussed in this study. In other words, W-C ratio, C-G ratio, and FA-B ratio were fixed for all samples.

Fig. 2 shows the detailed process of sample preparation and testing. Firstly, the gangue, fly ash, and cement were mixed and stirred for 60 s based on Table 2. Secondly, pure water was added and evenly mixed to form a filling slurry with a certain fluidity, then the weighed polymer material was stirred for 120 s, so that the polymer was evenly dispersed inside the slurry. Thirdly, the mixture was loaded into a cylinder mold with a volume of 50 mm × 100 mm. After 1 d of indoor curing at normal temperature, the mold was removed. According to the GB/T50080-2016 Chinese national standard for test method of performance on ordinary fresh concrete (China Academy of Building Research), the sample was put into the standard curing room with a temperature of (20 ± 2)°C and a humidity of (95 ± 2)% for 7 d, 14 d, or 28 d curing. Finally, UCS and AE tests on samples with different curing ages were conducted.

Table 2. Test scheme

No.	P-C ratio	W-C ratio	C-G ratio	FA-B ratio
Blank	0	0.5	0.4	0.6
A1	0.15			
A2	0.20			
A3	0.25			
A4	0.30			

2.3. Uniaxial compressive strength test

According to the ASTM C39 standard, the electro-hydraulic servo universal testing machine (SHT-4206, SANS, China) was employed to conduct the UCS test, and the loading rate was set at 0.1 mm/min. During the loading process, the experimental data were automatically recorded by the testing system, including load, displacement, and time. At the same time, the stress–strain curve was drawn, and the UCS of the sample was obtained. Three tests were repeated for each proportioning of the sample, and the average value was calculated as the final UCS of the proportioning of the sample.

2.4. Acoustic emission test

During the UCS test, the AE monitoring system developed by the Physical Acoustics Corporation was used to collect the AE signals generated by the sample breaking. The acquisition rate of the AE signal was set as 2 MHz, and the AE threshold was set as 45 dB. A total of 6 emission sensors were installed on the sample surface, as shown in Fig. 2. The coupling agent Vaseline was used between the sensor and the sample surface, and hot-melt adhesive was used to ensure the good contact.

3. Results and discussion

3.1. Results of UCS tests

3.1.1. UCS results of PCPB samples

Fig. 3 shows the UCS results of PCPB samples with different P-C ratios and curing ages. When the curing age is 7 d, the UCS values of the samples with a P-C ratio of 0, 0.15, 0.20, 0.25, and 0.30 are 4.59, 6.43, 8.18, 9.63, and 9.88 MPa,

Fig. 2. Test process.

respectively. Compared with the blank group (the sample with the P-C ratio of 0), the UCS values of PCPB samples with the P-C ratio of 0.15, 0.20, 0.25, and 0.30 are increased by 40.09%, 78.21%, 109.25%, and 115.25%, respectively. When the curing age is 14 d, the UCS values of PCPB samples with the P-C ratio of 0, 0.15, 0.20, 0.25, and 0.30 are 6.97, 8.62, 9.97, 11.78, and 16.47 MPa, respectively. Compared with samples in the blank group, the UCS values of the samples with the P-C ratio of 0.15, 0.20, 0.25, and 0.30 are increased by 23.67%, 43.04%, 69.01%, and 136.3%, respectively. When the curing age is 28 d, the corresponding UCS values of the samples with the P-C ratio of 0, 0.15, 0.20, 0.25, and 0.30 are 10.76, 12.68, 14.2, 16.53, and 21.8 MPa, respectively. Compared with samples in the blank group, the UCS values of PCPB samples with the P-C ratio of 0.15, 0.20, 0.25, and 0.30 are increased by 17.84%, 31.97%, 53.62%, and 102.6%, respectively. The above results show that the waterborne epoxy resin lotion can effectively improve the mechanical strength of PCPB samples, and with the increase of the P-C ratio, the promotion effect on the mechanical strength is more significant. This is mainly because the waterborne epoxy resin lotion is an effective polymer binder, and the adhesion between aggregates can be improved after the waterborne epoxy resin lotion is added to PCPB samples. By fitting the UCS of PCPB samples under different P-C ratios, it can be found that the UCS of PCPB samples under each curing age presents a relationship with the P-C ratio by $y = ax^2 + bx + c$, and the fitting coefficients (R^2) are greater than 0.9. It indicates that the UCS of PCPB samples has a high correlation with the P-C ratio. Besides, the curing age also has an important impact on the mechanical strength of PCPB. With the growth of curing age, the cementitious materials in PCPB samples gradually undergo hydration reaction, fill the voids between aggregates, and improve their co-

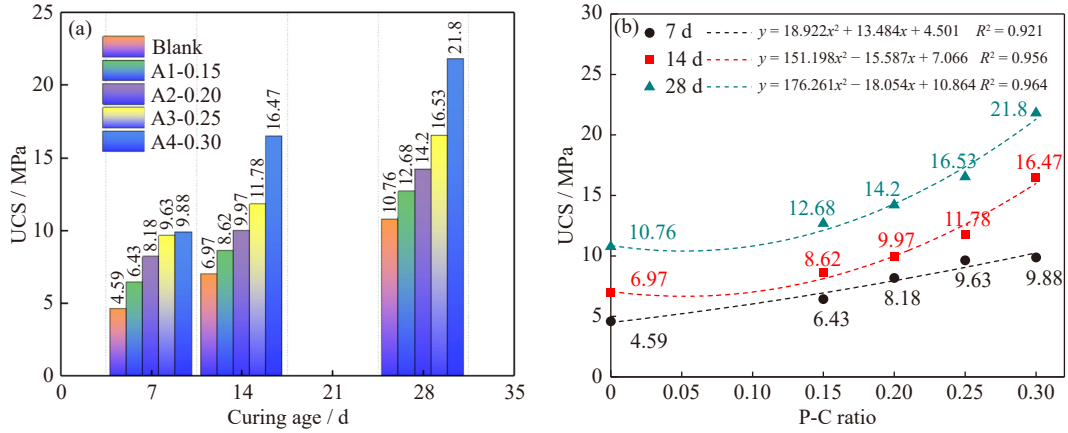

Fig. 3. Uniaxial compressive strength test results of PCPB: (a) relationship between UCS and curing age; (b) relationship between UCS and P-C ratio.

hesiveness, resulting in the continuous increase of UCS in PCPB samples. It is worth noting that the increasing effect of polymer on the mechanical strength gradually decreases with the increase in the curing age. Taking the PCPB sample with a P-C ratio of 0.15 as an example, the increase rate of polymer on the UCS in PCPB samples with the curing ages of 7, 14, and 28 d is 40.09%, 23.67%, and 17.84%, respectively. This shows that the gain effect of waterborne epoxy resin lotion on the mechanical strength of the sample mainly occurs in the middle and early curing stages.

3.1.2. Stress–strain curves of PCPB samples

Fig. 4 shows the stress–strain curves of PCPB samples with different P-C ratios under curing ages of 7, 14, and 28 d. Since the curves of PCPB samples with the same proportion at the same curing age are similar, a typical curve is drawn in the figure. Under uniaxial load, the stress–strain curve of PCPB samples experiences four stages: micropore compaction stage (section O–A), elastic deformation stage (section A–B), plastic deformation stage (section B–C), and failure instability stage (section C–D). In the micropore compaction stage, the small pores in the sample are gradually closed under the action of axial compressive stress, and the compactness of the sample is increasing. At this time, the stress–strain curve is concave. With the increase of load, after the micropores are closed, the sample begins to enter the elastic deformation stage. In this process, the sample mainly undergoes elastic deformation, and the stress–strain curve is almost straight. When the shear stress applied on the fracture surface exceeds its friction force, the microcracks are gradually developed, while the core area inside the sample is still intact. In the plastic deformation stage, the tensile stress inside the sample increases rapidly. Under the influence of the tip effect, secondary tensile cracks appear at both ends of the crack and expand rapidly until the main crack runs through the sample. At this time, the sample loses its deformation resistance. This process lasts for a short time and the crack develops rapidly. When the stress applied to the sample reaches the peak strength, the failure and instability stage is reached. Although the overall structure of the sample is destroyed and a large number of macro cracks are developed, it still has a certain residual strength.

Fig. 5 shows the relationship between peak strain and P-C ratios of PCPB samples with different curing ages. With the increase of curing age, the peak strain of PCPB samples decreases first and then increases. For example, the peak strain of samples in the blank group at the curing ages of 7, 14, and 28 d is 1.112×10^{-2}, 1.011×10^{-2}, and 1.061×10^{-2}, respectively. Due to the high internal moisture content of PCPB samples and the low hydration degree of raw materials in the early curing period, a small number of hydration products and a low cohesive force of materials are caused, and plastic deformation is dominant in the compression process. When

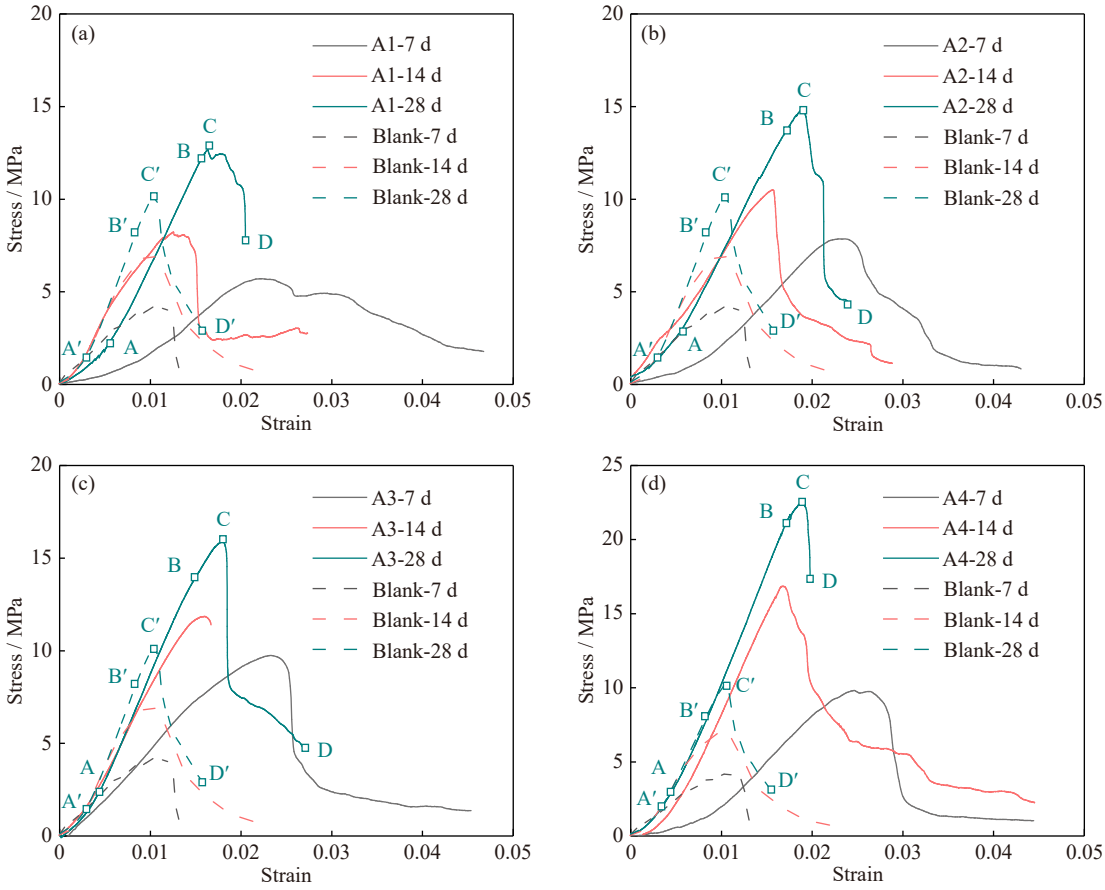

Fig. 4. Stress–strain curves of PCPB during different curing ages: (a) blank and A1; (b) blank and A2; (c) blank and A3; (d) blank and A4.

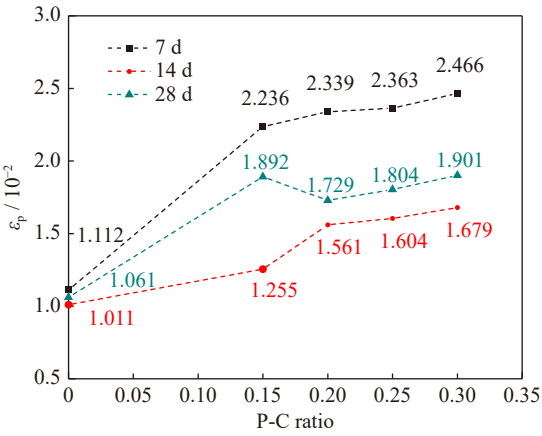

Fig. 5. Relationship between peak strain (ε_p) and P-C ratio of samples with different curing ages.

the curing age is 14 d, the hydration reaction of the material consumes the internal free water, and the hydration products generated by hydration improve the cohesion between the aggregates. Consequently, the hardness and brittleness of the sample increase, while its plasticity decreases. When the curing age is 28 d, the basic hydration of raw materials is completed. The hydration products improve the cohesiveness of the aggregate and also improve its compactness. Moreover, the cross-linking interaction between polymer and cement hydration products increases the material's resistance to deformation and damage, and its peak strain slightly increases compared with that for 14 d. With the incorporation of the waterborne epoxy plot, the peak strain values of the PCPB sample increase significantly. For example, when the P-C ratio increases from 0 to 0.30, the peak strain of the PCPB sample with a curing age of 7 d increases from 1.112×10^{-2} to 2.466×10^{-2}, the peak strain of the PCPB sample with a curing age of 14 d increases from 1.011×10^{-2} to 1.679×10^{-2}, and the peak strain the PCPB sample with a curing age of 28 d changes from 1.061×10^{-2} to 1.901×10^{-2}. The peak strains of the PCPB samples in A2, A3, and A4 groups are much larger than those of the blank group. According to Section 3.1.1, the waterborne epoxy plot can not only greatly improve the mechanical strength of the PCPB sample, but also increase its peak strain.

3.1.3. Macro crack development characteristics

Fig. 6 shows the macro crack development characteristics of PCPB samples with different P-C ratios under the curing age of 28 d. It can be seen that under the action of uniaxial stress, the failure cracks of the sample mostly develop along the axial direction, belonging to multi-level splitting cracks, and the main cracks can run through the sample. With the increase in the P-C ratio, the angle between the fracture surface and the horizontal line increases gradually. For example, the main fracture angles (θ) of samples with the P-C ratio of 0, 0.15, 0.20, 0.25, and 0.30 are 74°, 78°, 82°, 87°, and 88°, respectively. In addition, the failure mode of the sample is also changed from shear failure to splitting failure. Besides the main crack, there are also a large number of small cracks distributed around the main crack on its surface. However, with the increase in the P-C ratio, the number of small cracks on its surface also decreases, and the block that fell from the sample is more broken.

3.2. Acoustic emission test results

The stress–strain curve can be used to qualitatively ana-

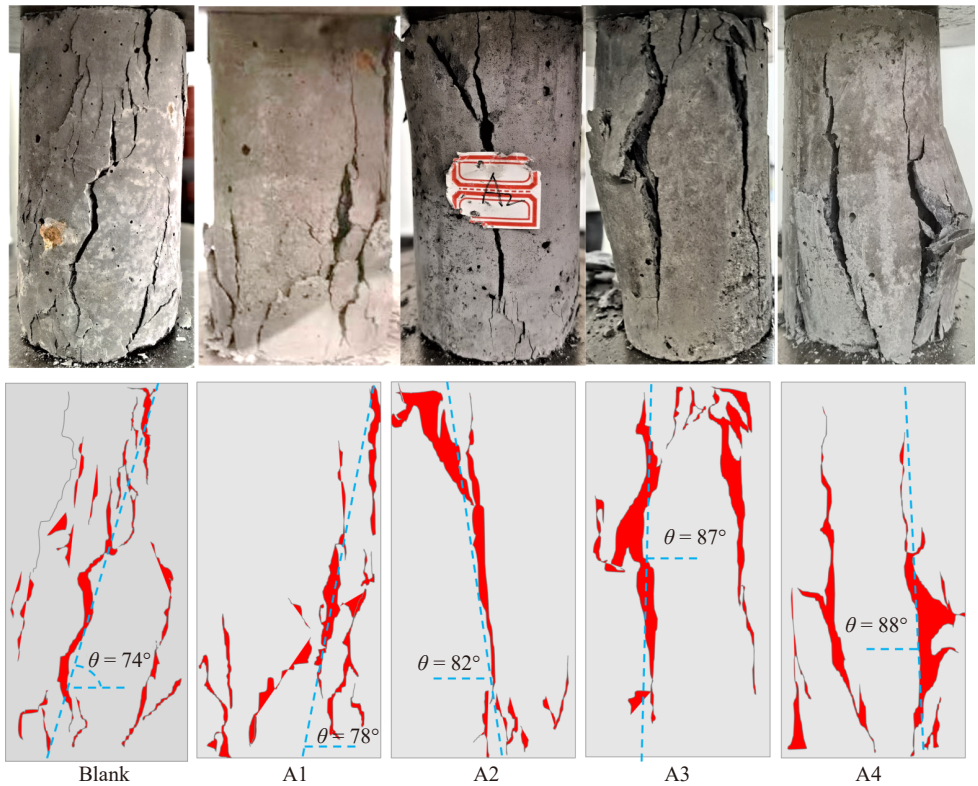

Fig. 6. Macroscopic crack development characteristics of the PCPB samples.

lyze the macro failure process of PCPB samples, while the fracture mechanism of its mesostructure cannot be intuitively and quantitatively studied [44]. The macro mechanical characteristics of PCPB samples are the result of the qualitative change caused by its micromechanical effect under the action of the load. Therefore, AE technology was used to monitor PCPB samples with a curing age of 28 d in real time to obtain the micro-mechanical characteristics of the sample under the load, and then AE parameters were used to characterize the micromechanical properties and fracture mechanism of PCPB samples.

3.2.1. AE properties of PCPB samples at different loading stages

Fig. 7 shows the curves of AE energy, cumulative energy, AE counts, cumulative AE counts, and stress versus loading time during the uniaxial compression of PCPB samples. According to the change law of AE energy and AE count with time, the failure process of PCPB samples can be roughly di-

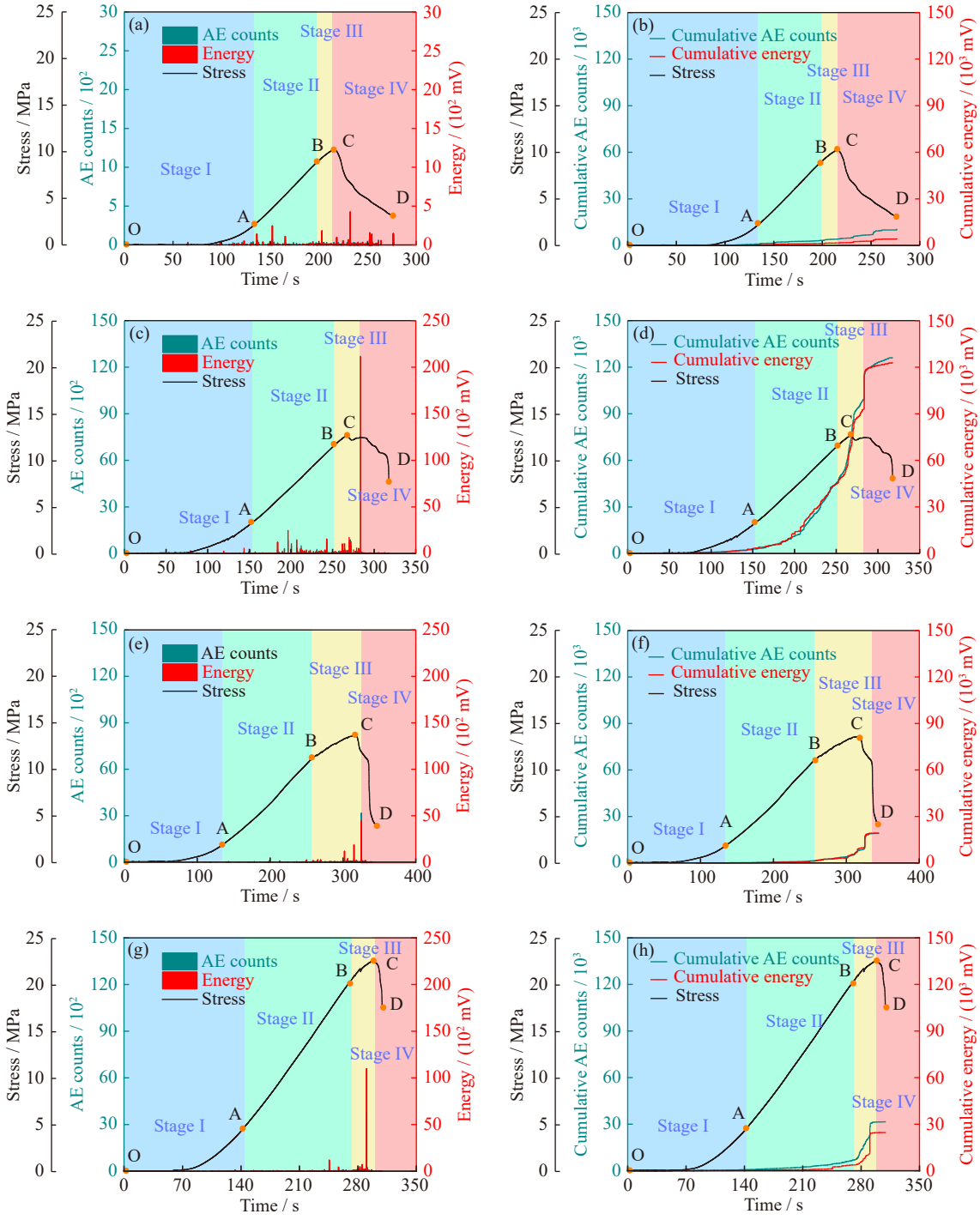

Fig. 7. Variations of AE energy, AE counts, and stress during different loading time: (a) AE counts and energy and (b) cumulative AE counts and energy of blank group; (c) AE counts and energy and (d) cumulative AE counts and energy of A1 group; (e) AE counts and energy and (f) cumulative AE counts and energy of A2 group; (g) AE counts and energy and (h) cumulative AE counts and energy of A4 group.

vided into four stages: quiet period (stage I), slow growth period (stage II), rapid growth period (stage III), and remission period (stage IV). It is worth noting that these four stages are consistent with the four stages of the stress–strain curve. Compared with samples in the blank group, the AE energy and AE count of PCPB samples with the P-C ratio of 0.15, 0.20, 0.25, and 0.30 are significantly increased, which also indicates that the hardness of PCPB samples is improved after polymer incorporation.

At the initial AE stage, the AE event is in a quiet period. At this time, the micropores and microcracks in the sample are gradually compacted under the action of the initial load, and a small number of elastic waves and energy are generated [45]. Since the AE energy generated by the compaction and closure of the micropores and microcracks is far less than the AE energy generated by the crack propagation [46], the AE count and AE energy in this stage are less, and the AE energy is generally lower than 50 mV. As the loading continues, the elastic deformation stage of the sample is reached, and the slow growth period of the AE event is also entered. At this time, the microcracks are continuously generated and slowly expand, while no macro cracks are produced in the sample. Therefore, the AE energy and AE count increase slowly. After entering the plastic deformation stage, the rapid growth stage of the AE event is entered. At this time, the cracks in the sample expand rapidly, and under the influence of the tip effect, the secondary cracks are generated and expand continuously [47]. When the tensile stress of the microcracks is greater than the adhesive force between the aggregate and the cementitious material, the macro fracture occurs in the sample, and the elastic wave and energy were rapidly released, and a large number of AE counts and AE energy are generated. As a result, the accumulated AE count and the accumulated AE energy rise rapidly in an almost straight line. It is worth noting that compared with the blank group, the AE count and AE energy of PCPB samples at this stage are significantly higher, and the slope of the cumulative AE count and cumulative AE energy curve is also larger. When the stress reaches the peak value, the macro fracture inside the sample is complete, the number of microcracks is continuously reduced, and the generated elastic wave energy, the AE count, and AE energy rapidly decrease. At this time, the remission period of AE events is also reached.

3.2.2. Crack classification at different loading stages

The mechanical properties and failure laws of PCPB samples under uniaxial load are analyzed by AE energy and AE counting, but the failure mechanism of PCPB samples, especially the failure modes at different AE stages, is still unclear. To this end, the RA (rise angle) value and AF (average frequency) value were used for distinguishing the tensile crack and shear crack (Fig. 8) [48–50]. Fig. 9 shows the division form of RA and AF values. The RA and AF values can be calculated by the following equations:

$$\mathrm{RA} = \mathrm{RT}/A \tag{1}$$

$$\mathrm{AF} = C/D \tag{2}$$

where RT is the rise time, A is the amplitude, D is the duration of the AE waveform, and C is the ringing counts.

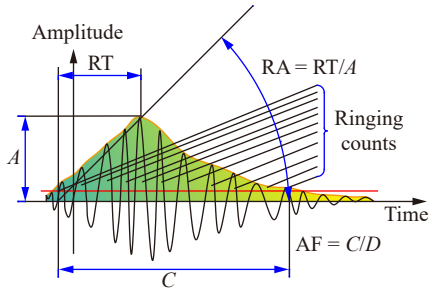

Fig. 8. Graphical representations of AE characteristic parameters [48–49].

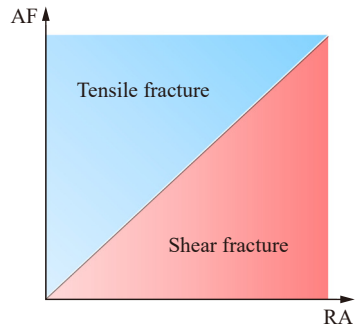

Fig. 9. Basis chart of fracture mode classification [48–49].

In this study, a straight line AF = 2/3RA is used to divide the failure mode of the sample [48–50]. Fig. 10 is a scatter diagram of RA–AF in different loading stages and its proportion. In this figure, the AE events ratio represents the proportion of AE events in each stage to the total number of events; the tensile cracks ratio represents the proportion of data above the dividing line in each stage; the shear cracks ratio represents the proportion of data below the dividing line in each stage.

Fig. 10 shows that shear cracks and tensile cracks occur in all samples at each loading stage, and there is an obvious difference in the number of cracks at different loading stages. However, the tensile cracks are the main failure cracks, which indicates that tensile failure mainly occurs in the PCPB samples during the loading process [51]. At the low load stage in the early test, some low-frequency tensile cracks are generated, and the peak frequency of AE signals generated in stages I and II are almost distributed around 50 kHz. From stage III, AE signals with peak frequencies around 30 and 120 kHz are rapidly generated. As the applied load increases, the AE data in the AF–RA map changes from the distribution along the RA direction to that along the AF direction [52]. In the quiet period (stage I) of the initial loading stage, the cracks of the sample are the least, accounting for about 3% of the whole loading stage, and the peak frequency of the AE signal is mainly distributed at about 50 kHz. At this time, the sample is in the stage of micropore compaction stage (section O–A), there is no significant damage inside the sample, and the original micropores in the sample are squeezed under the external force, resulting in tensile failure on both sides of the pore wall. Therefore, the tensile failure is the main failure mode of the sample at this stage [53]. In the

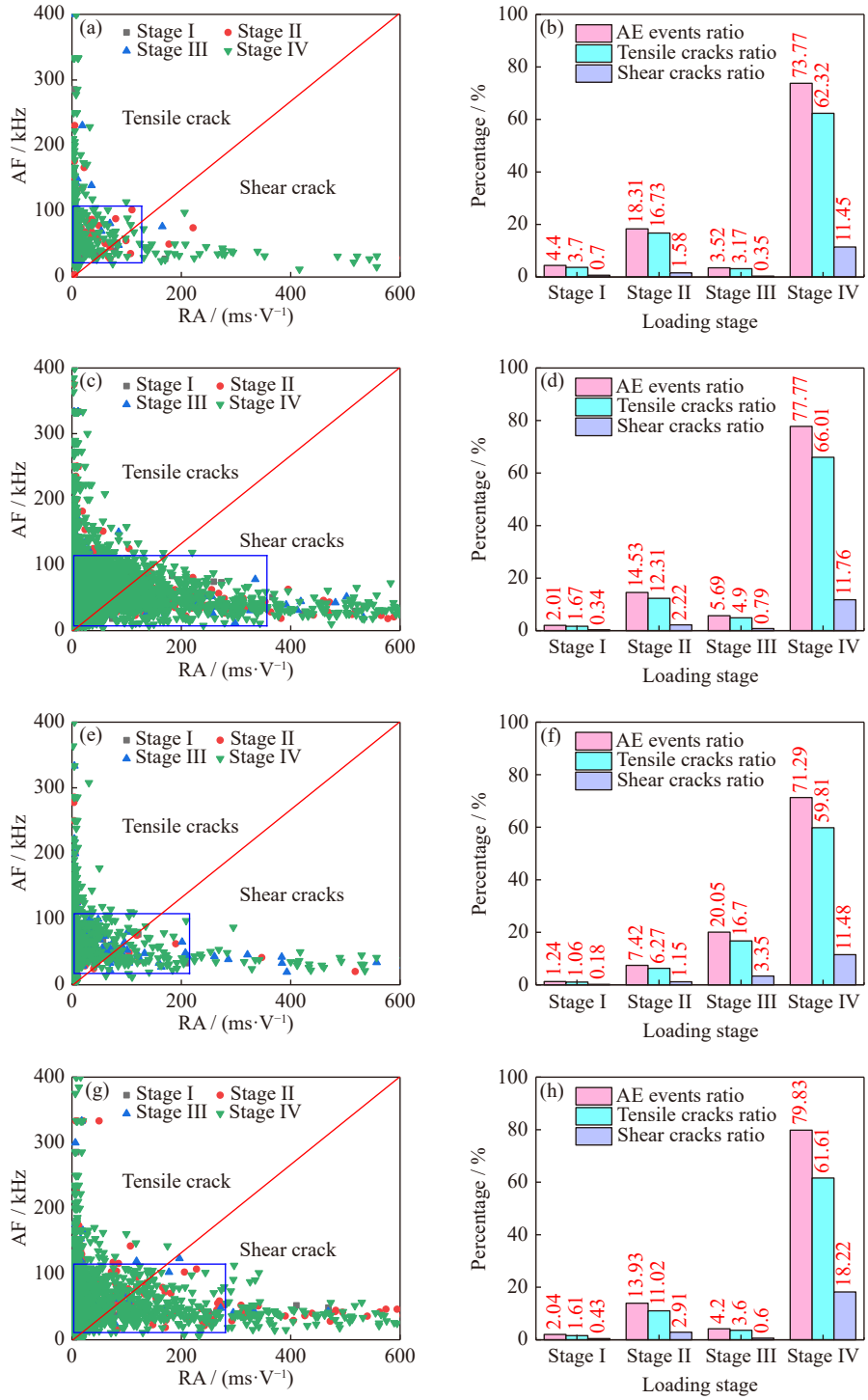

Fig. 10. Cracking mode classification based on RA and AF indices under different loading stages: (a) cracking mode classification and (b) crack classification ratio of blank group; (c) cracking mode classification and (d) crack classification ratio of A1 group; (e) cracking mode classification and (f) crack classification ratio of A2 group; (g) cracking mode classification and (h) crack classification ratio of A4 group.

slow growth period (stage II), the aggregate and cemented matrix first deform together, and some micro cracks are developed at the transition interface between them. Therefore, a certain shear failure occurs in this stage. During the rapid growth period (stage III), the main crack of the sample is gradually formed. When the stress reaches the limit value, splitting failure occurs in the sample. In the remission period (stage IV), the sample is continuously damaged along the main crack until it is completely destroyed. At this stage, a large number of shear cracks and tensile cracks are generated inside the sample.

3.2.3. Spatial evolution of AE

The iterative algorithm based on the P-wave arrival time and position by AE sensors at different positions can realize the three-dimensional spatial location of AE events, thus intuitively reflecting the evolution process and spatial location

of damage cracks during the loading. Fig. 11 shows the temporal and spatial evolution of AE events of PCPB samples. During the test, when the same AE event is obtained by more than three AE sensors, the spatial position of damage cracks can be determined. Therefore, the number of AE events in Fig. 11 is significantly less than that in Figs. 7 and 10.

During early loading (i.e., the stress is below 50%σ_{max}, where σ_{max} is the peak stress), the sample is mainly in the void compaction stage (section O–A) and the initial elastic stage (section A–B), and no obvious deformation or damage occurs to the sample in this two stages. At this time, the original microcracks and micro-voids of the sample are compacted. Therefore, there are few AE locating points, which are randomly distributed inside the sample. When the stress increases to 80%σ_{max}, the number of AE locating points increases gradually. At this stage, a small number of AE locating points begin to converge. At this time, the sample is mainly in the late elastic stage, and a small number of new cracks begin to appear in the sample, with local stress concentration. When the stress reaches 90%σ_{max}, AE locating points are further increased with a higher concentration degree. For samples in the blank group, AE locating points are mainly concentrated in the upper area, with a low concentration degree. However, the AE locating points of A1, A2, and A4 are mainly concentrated in the lower area, where an internal crack is formed near the main crack. This may be caused by the aggregate settlement segregation, which occurs in the process of mold loading vibration [54]. As a result, the upper part of the CPB (blank group) specimen has less aggregate and poor strength, which is the first to be destroyed during loading. After adding the polymer, the stability of the PCPB slurry can be enhanced, and higher strength of

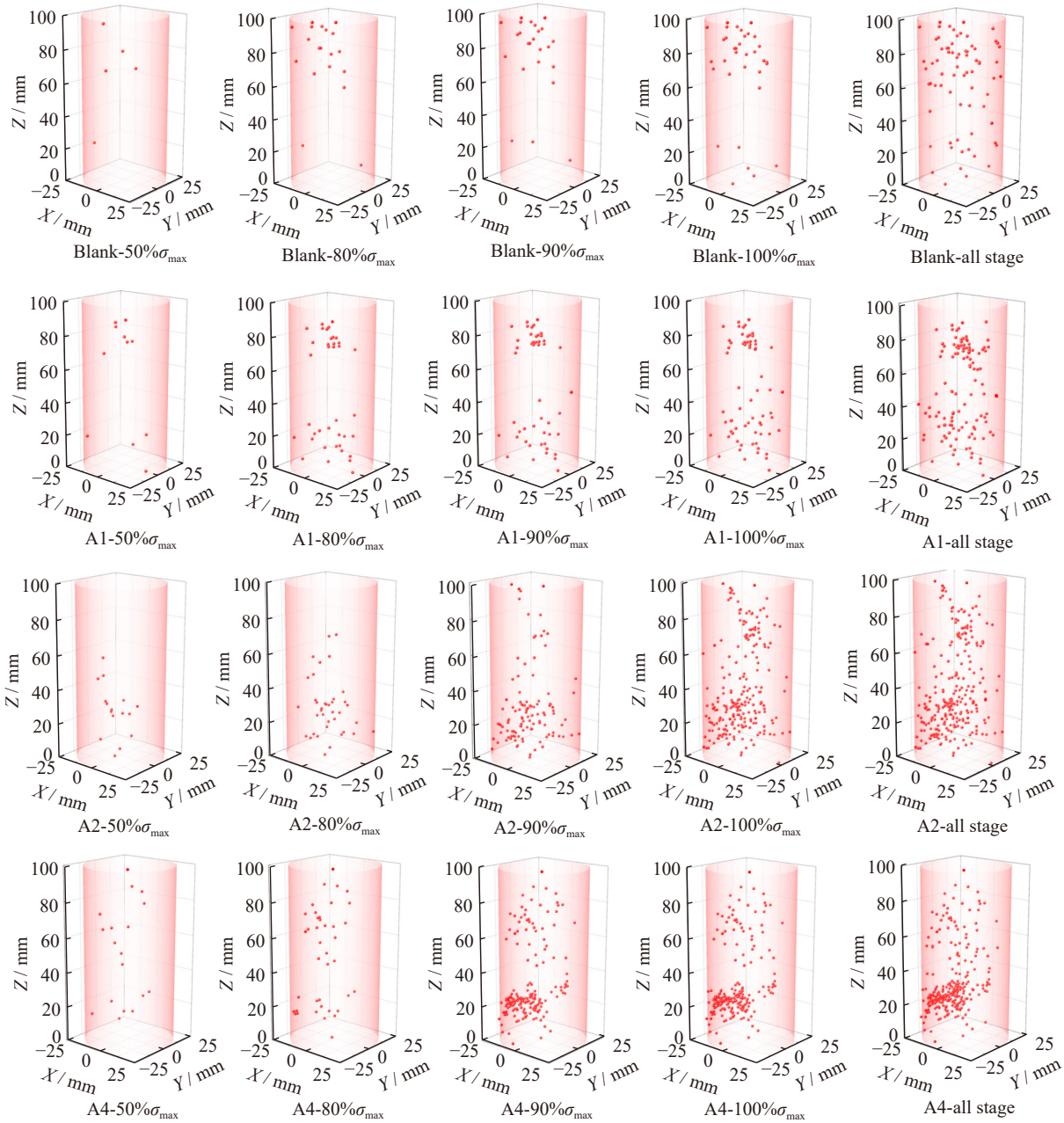

Fig. 11. Space-time characteristics of AE response of PCPB samples.

the specimen can be obtained, thus changing the failure position of the PCPB during the loading. At this stage, the microcracks begin to aggregate in the direction of the unpenetrated main crack. When the stress reaches 100%σ_{max}, the number of AE events increases sharply, and several concentrated areas also appear at AE locating points in the sample. This is mainly caused by the connection of micro cracks and the formation of macro main cracks, and the aggregation position of AE locating points is relatively consistent with the main fracture position of the sample (Fig. 6). At this stage, the number of AE locating points increases slightly, which is different from the sharp increase of AE counting. This phenomenon is caused by the huge energy release during sample failure. It can be inferred that significant damage occurs before the brittle failure of the sample, and the failure involves the macro change of damage accumulation to some extent. Therefore, AE location technology accurately reflects the spatial evolution of internal damage of samples during loading. The comparison of AE location points between PCPB samples and blank samples shows that due to the bonding effect of the waterborne epoxy plot, PCPB samples have more AE locating points than blank samples, and the larger the P-C ratio, the more AE locating points. This result is consistent with the cumulative AE count and energy discussed in Section 3.2.1.

4. Conclusions

(1) Waterborne epoxy lotion is a good binder, which can effectively improve the strength and deformation resistance of PCPB samples; with the increase in the P-C ratio, the promoting effect of waterborne epoxy lotion on mechanical strength is more significant.

(2) The stress–strain curve of PCPB samples can be divided into four stages: micropore compaction stage, elastic deformation stage, plastic deformation stage, and failure instability stage. The AE event is in the quiet period during the pore compaction stage. In the elastic deformation stage, the number of AE events increases slowly. Near the peak stress, the number of AE events increases rapidly, causing internal damage to the sample. When the sample failure occurs, and the AE counting and amplitude rapidly increase to the peak value.

(3) In the whole loading stage, both shear cracks and tensile cracks are generated in PCPB samples, while tensile cracks are the main failure cracks, that is, tensile failure is the main failure mode in the PCPB samples during loading. What's more, the AE location technology can precisely reflect the crack expansion and the spatial evolution of internal damage during loading.

5. Future work

This paper focuses on the influence of P-C ratio on the mechanical strength of PCPB, and discusses the meso-damage characteristics of PCPB by AE test, but it is difficult to visually demonstrate the development process and mechanism of cracks. Future studies need to use a Computed Tomography to scan PCPB during different loading stages, and then, use three-dimensional reconstruction software to obtain internal damage cracks at different loading stages, so as to intuitively express the mechanism of strengthening the mechanical properties of PCPB.

Acknowledgements

This work was supported by the National Natural Science Foundation of China (Nos. 52022107, 52174128, and 52104103), the Natural Science Foundation of Jiangsu Province (Nos. BK20190031 and BK20210499), the "Tianshan Innovation Team Plan" Project (No. 2021D14016), the Xinjiang Key Research and Development Special Project (No. 2022B03028-3), and the Xinjiang Central Guidance Local Fund Project.

Conflict of Interest

Nan Zhou is a youth editorial board member for this journal and was not involved in the editorial review or the decision to publish this article. The authors declare no conflict of interest.

References

[1] J.M. Li, Y.L. Huang, S.Y. Ouyang, *et al*., Transparent characterization and quantitative analysis of broken gangue's 3D fabric under the bearing compression, *Int. J. Min. Sci. Technol.*, 32(2022), No. 2, p. 335.

[2] X.J. Deng, Y. Li, F. Wang, *et al*., Experimental study on the mechanical properties and consolidation mechanism of microbial grouted backfill, *Int. J. Min. Sci. Technol.*, 32(2022), No. 2, p. 271.

[3] T.Z. Gao and F. He, Research of geological environment remediation and reconstruction of coal mining area in western of Shijiazhuang city, China, *Adv. Mater. Res.*, 726-731(2013), p. 1628.

[4] Y. Shi, L. Cheng, M. Tao, S.S. Tong, X.J. Yao, and Y.F. Liu, Using modified quartz sand for phosphate pollution control in cemented phosphogypsum (PG) backfill, *J. Cleaner Prod.*, 283(2021), art. No. 124652.

[5] X.J. Deng, J.X. Zhang, B. Klein, B. de Wit, and J.W. Zhang, Time-dependent lateral pressure of the filling barricade for roadway cemented backfill mining technology, *Mech. Time-Depend. Mater.*, 24(2020), No. 1, p. 41.

[6] Q. Sun, J.X. Zhang, N. Zhou, and W.Y. Qi, Roadway backfill coal mining to preserve surface water in Western China, *Mine Water Environ.*, 37(2018), No. 2, p. 366.

[7] A.G. Doven and A. Pekrioglu, Material properties of high volume fly ash cement paste structural fill, *J. Mater. Civ. Eng.*, 17(2005), No. 6, p. 686.

[8] R. Wu, P.H.S.W. Kulatilake, H. Luo, and K. Zhao, Design of the key bearing layer and secondary mining technology for previously mined areas of small coal mines, *Rock Mech. Rock Eng.*, 53(2020), No. 4, p. 1685.

[9] Y. Chen, S.Q. Ma, and Q.J. Cao, Extraction of the remnant coal pillar in regular and irregular shapes: A case study, *J. Loss Prev. Process Ind.*, 55(2018), p. 191.

[10] Y. Yu, K.Z. Deng, and S.E. Chen, Mine size effects on coal pil-

lar stress and their application for partial extraction, *Sustainability*, 10(2018), No. 3, art. No. 792.
[11] R.H. Su and H.S. Shen, Physical characteristics of section coal and rock pillars under roof shock disturbances from goaf, *Front. Phys.*, 8(2020), art. No. 223.
[12] S. Guo, M. Fall, and S. Haruna, Interface shear behavior of cementing underground mine backfill, *Int. J. Geomech.*, 20(2020), No. 12, art. No. 04020230.
[13] L. Liu, J. Xin, C. Huan, *et al*., Effect of curing time on the mesoscopic parameters of cemented paste backfill simulated using the particle flow code technique, *Int. J. Miner. Metall. Mater.*, 28(2021), No. 4, p. 590.
[14] J.H. Qin, J. Zheng, and L. Li, Experimental study of the shrinkage behavior of cemented paste backfill, *J. Rock Mech. Geotech. Eng.*, 13(2021), No. 3, p. 545.
[15] C.C. Qi, and A. Fourie, Cemented paste backfill for mineral tailings management: Review and future perspectives, *Miner. Eng.*, 144(2019), art. No. 106025.
[16] L. Cui and M. Fall, Multiphysics modeling and simulation of strength development and distribution in cemented tailings backfill structures, *Int. J. Concr. Struct. Mater.*, 12(2018), No. 1, art. No. 25.
[17] X.J. Deng, J.X. Zhang, B. Klein, N. Zhou, and B. deWit, Experimental characterization of the influence of solid components on the rheological and mechanical properties of cemented paste backfill, *Int. J. Miner. Process.*, 168(2017), p. 116.
[18] D. Ma, S.B. Kong, Z.H. Li, Q. Zhang, Z.H. Wang, and Z.L. Zhou, Effect of wetting-drying cycle on hydraulic and mechanical properties of cemented paste backfill of the recycled solid wastes, *Chemosphere*, 282(2021), art. No. 131163.
[19] L.H. Yang, H.J. Wang, A.X. Wu, *et al*., Effect of mixing time on hydration kinetics and mechanical property of cemented paste backfill, *Constr. Build. Mater.*, 247(2020), art. No. 118516.
[20] B. Ercikdi, G. Külekci, and T. Yılmaz, Utilization of granulated marble wastes and waste bricks as mineral admixture in cemented paste backfill of sulphide-rich tailings, *Constr. Build. Mater.*, 93(2015), p. 573.
[21] X.G. Zhang, J. Lin, J.X. Liu, F. Li, and Z.Z. Pang, Investigation of hydraulic-mechanical properties of paste backfill containing coal gangue-fly ash and its application in an underground coal mine, *Energies*, 10(2017), No. 9, art. No. 1309.
[22] X. Chen, X.Z. Shi, J. Zhou, X.H. Du, Q.S. Chen, and X.Y. Qiu, Effect of overflow tailings properties on cemented paste backfill, *J. Environ. Manage.*, 235(2019), p. 133.
[23] B. Ercikdi, F. Cihangir, A. Kesimal, H. Deveci, and İ. Alp, Utilization of industrial waste products as pozzolanic material in cemented paste backfill of high sulphide mill tailings, *J. Hazard. Mater.*, 168(2009), No. 2-3, p. 848.
[24] E. Yilmaz, Stope depth effect on field behaviour and performance of cemented paste backfills, *Int. J. Min. Reclam. Environ.*, 32(2018), No. 4, p. 273.
[25] R.V. de la Villa, R. García, S. Martínez-Ramírez, and M. Frías, Effects of calcination temperature and the addition of ZnO on coal waste activation: A mineralogical and morphological evolution, *Appl. Clay Sci.*, 150(2017), p. 1.
[26] E.H. Kadri, S. Kenai, K. Ezziane, R. Siddique, and G. De Schutter, Influence of metakaolin and silica fume on the heat of hydration and compressive strength development of mortar, *Appl. Clay Sci.*, 53(2011), No. 4, p. 704.
[27] C.J. Zhou, L.L. Chen, S.P. Zheng, Y.X. Xu, and D.C. Feng, Rheological, mechanical, and abrasion characteristics of polymer-modified cement mortar and concrete, *Can. J. Civ. Eng.*, 47(2020), No. 11, p. 1226.
[28] R. Wang, X. X. Shi, and P. M. Wang, Recent research on polymer-modified cement mortar in China, *Adv. Mater. Res.*, 687(2013), p. 57.
[29] J.P. Xiong, J.X. Deng, W. Hao, and R.P. Qin, Study on modification mechanism of the polymer modified cement concrete, *Appl. Mech. Mater.*, 357-360(2013), p. 998.
[30] Y. Tian, X.Y. Jin, N.G. Jin, R.Y. Zhao, Z.J. Li, and H.Y. Ma, Research on the microstructure formation of polyacrylate latex modified mortars, *Constr. Build. Mater.*, 47(2013), p. 1381.
[31] J. Mirza, M. Mirza and R. Lapointe, Laboratory and field performance of polymer-modified cement-based repair mortars in cold climates, *Constr. Build. Mater.*, 16(2002), No. 6, p. 365.
[32] W. Mahmood, A. Mohammed, and K. Ghafor, Viscosity, yield stress and compressive strength of cement-based grout modified with polymers, *Results Mater.*, 4(2019), art. No. 100043.
[33] X.J. Zhang, M.R. Du, H.Y. Fang, M.S. Shi, C. Zhang, and F.M. Wang, Polymer-modified cement mortars: Their enhanced properties, applications, prospects, and challenges, *Constr. Build. Mater.*, 299(2021), art. No. 124290.
[34] Z. Naseem, E. Shamsaei, K. Sagoe-Crentsil, and W.H. Duan, Antifoaming effect of graphene oxide nanosheets in polymer-modified cement composites for enhanced microstructure and mechanical performance, *Cem. Concr. Res.*, 158(2022), art. No. 106843.
[35] Y.P. Liu, J.T. Wang, S.G. Hu, S. Cao, and F.Z. Wang, Enhancing the mechanical behaviour of concretes through polymer modification of the aggregate-cement paste interface, *J. Build. Eng.*, 54(2022), art. No. 104605.
[36] Q. Liu, Z.Y. Lu, X.S. Hu, *et al*., A mechanical strong polymer-cement composite fabricated by *in situ* polymerization within the cement matrix, *J. Build. Eng.*, 42(2021), art. No. 103048.
[37] G.L. Xue and E. Yilmaz, Strength, acoustic, and fractal behavior of fiber reinforced cemented tailings backfill subjected to triaxial compression loads, *Constr. Build. Mater.*, 338(2022), art. No. 127667.
[38] R. Li, Z. Leng, Y. Zhang, and X. Ma, Preparation and characterization of waterborne epoxy modified bitumen emulsion as a potential high-performance cold binder, *J. Cleaner Prod.*, 235(2019), p. 1265.
[39] S. Cao, E. Yilmaz, W.D. Song, E. Yilmaz, and G.L. Xue, Loading rate effect on uniaxial compressive strength behavior and acoustic emission properties of cemented tailings backfill, *Constr. Build. Mater.*, 213(2019), p. 313.
[40] Q.M. Xu, Y. Li, R.T. Xu, Y.M. Liu, and Y.M. Dong, Performance evaluation of waterborne epoxy resin modified emulsified asphalt mixtures for asphalt pavement pothole repair, *Constr. Build. Mater.*, 325(2022), art. No. 126709.
[41] Y. Li, Y.C. Guo, Z.G. Lyu, and X. Wei, Investigation of the effect of waterborne epoxy resins on the hydration kinetics and performance of cement blends, *Constr. Build. Mater.*, 301(2021), art. No. 124045.
[42] A. Abdukadir, Z.S. Pei, W. Yu, *et al*., Performance optimization of epoxy resin-based modified liquid asphalt mixtures, *Case Stud. Constr. Mater.*, 17(2022), art. No. e01598.
[43] L.X. Wang, J.W. Zhang, F.J. Wang, *et al*., Investigation on the effects of polyaniline/lignin composites on the performance of waterborne polyurethane coating for protecting cement-based materials, *J. Build. Eng.*, 64(2023), art. No. 105665.
[44] X.P. Song, Y.X. Hao, S. Wang, L. Zhang, W. Liu, and J.B. Li, Mechanical properties, crack evolution and damage characteristics of prefabricated fractured cemented paste backfill under uniaxial compression, *Constr. Build. Mater.*, 330(2022), art. No. 127251.
[45] J. Wang, J.X. Fu, W.D. Song, Y.F. Zhang, and Y. Wang, Mechanical behavior, acoustic emission properties and damage evolution of cemented paste backfill considering structural feature, *Constr. Build. Mater.*, 261(2020), art. No. 119958.
[46] S. Chakilam and L. Cui, Effect of polypropylene fiber content and fiber length on the saturated hydraulic conductivity of hydrating cemented paste backfill, *Constr. Build. Mater.*,

262(2020), art. No. 120854.
[47] T. Yılmaz, B. Ercikdi, and F. Cihangir, Evaluation of the neutralization performances of the industrial waste products (IWPs) in sulphide-rich environment of cemented paste backfill, *J. Environ. Manage.*, 258(2020), art. No. 110037.
[48] Y. Niu, X.P. Zhou, and F. Berto, Evaluation of fracture mode classification in flawed red sandstone under uniaxial compression, *Theor. Appl. Fract. Mech.*, 107(2020), art. No. 102528.
[49] Q.Q. Zheng, Y. Xu, H. Hu, J.W. Qian, Y. Ma, and X. Gao, Quantitative damage, fracture mechanism and velocity structure tomography of sandstone under uniaxial load based on acoustic emission monitoring technology, *Constr. Build. Mater.*, 272(2021), art. No. 121911.
[50] S. Shahidan, R. Pulin, N.M. Bunnori, and K.M. Holford, Damage classification in reinforced concrete beam by acoustic emission signal analysis, *Constr. Build. Mater.*, 45(2013), p. 78.
[51] N. Ouffa, M. Benzaazoua, T. Belem, R. Trauchessec, and A. Lecomte, Alkaline dissolution potential of aluminosilicate minerals for the geosynthesis of mine paste backfill, *Mater. Today Commun.*, 24(2020), art. No. 101221.
[52] D. Ouattara, M. Mbonimpa, A. Yahia, and T. Belem, Assessment of rheological parameters of high density cemented paste backfill mixtures incorporating superplasticizers, *Constr. Build. Mater.*, 190(2018), p. 294.
[53] M.B.C. Mangane, R. Argane, R. Trauchessec, A. Lecomte, and M. Benzaazoua, Influence of superplasticizers on mechanical properties and workability of cemented paste backfill, *Miner. Eng.*, 116(2018), p. 3.
[54] B. Yin, *Research on the Fly Ash Cemented Filling Materials and Its Modifcation and Further Application* [Dissertation], Taiyuan University of Technology, Taiyuan, 2018.